Supplementary information for

Multiscale fault-zone structures governed by earthquake rupture dynamics

Dezheng Zhao[1], Huihui Weng[1*], Qin Wang[1], Yijian Zhou[2], Han Chen[3]

1. State Key Laboratory for Mineral Deposits Research, School of Earth Sciences and Engineering, Nanjing University, Nanjing, China
2. Department of Earth Sciences, University of California, Riverside, California, U.S.A.
3. State Key Laboratory of Earthquake Dynamics, Institute of Geology, China Earthquake Administration, Beijing, China

Contents:

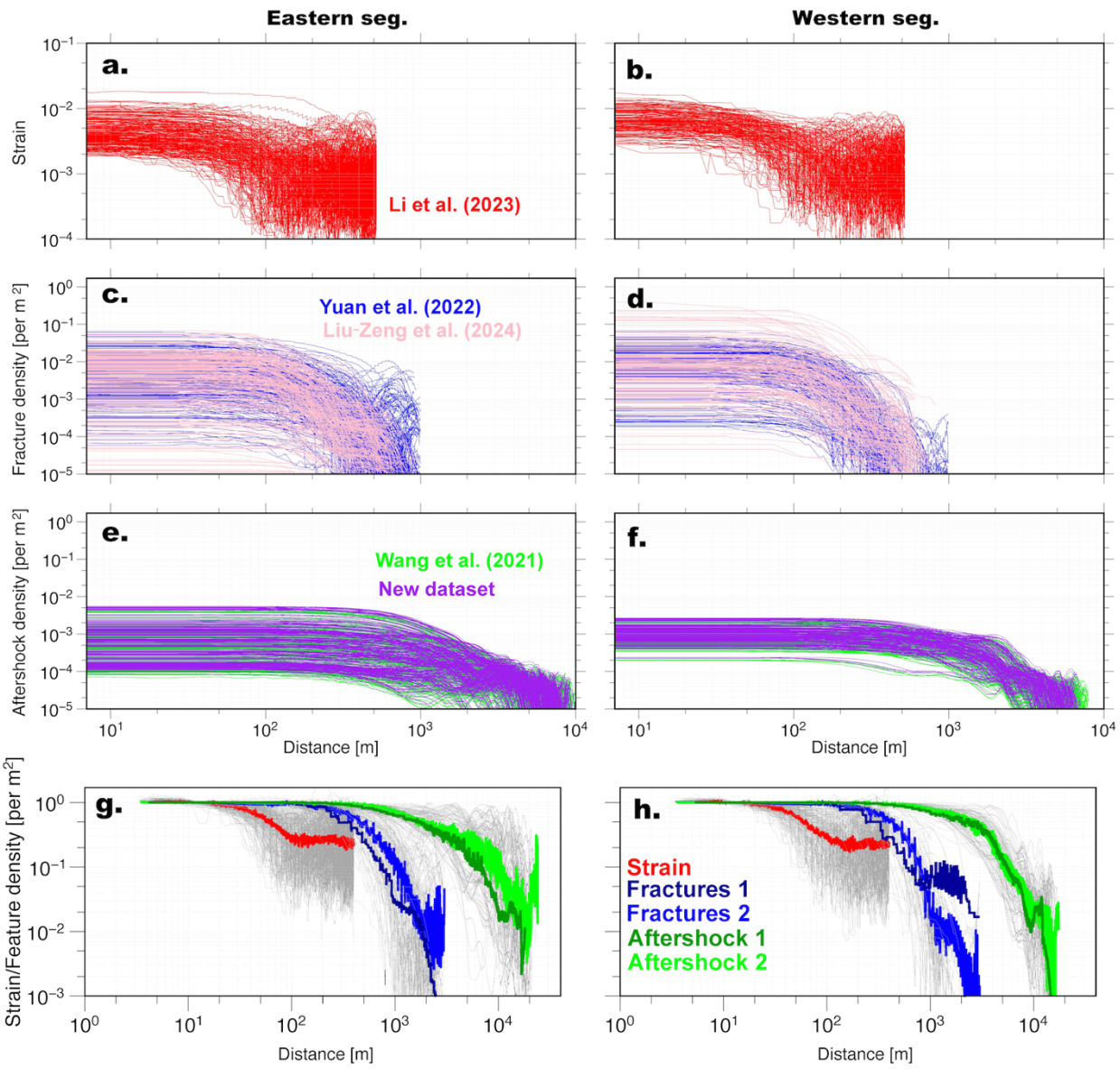

Figure S1. Profiles of surface shear strain (a, b), fracture density (c, d), aftershock density (e, f), and the corresponding stacking decay curves (g, h). Each curve in (a-f) corresponds to one profile (20 km long across the fault, every 140 m along the fault) with orientation perpendicular to the primary surface rupture of the Maduo earthquake. In c, d, e, and f, curves with different colors represent results from different independent datasets. The first and second columns are results for fault segments to the east and the west of the epicenter of the Maduo earthquake, respectively. In (g, h), stacked shear strain (red), fractures (blue from Yuan et al.[1], dark blue from Liu-Zeng et al.[2]), and relocated aftershocks (green from Wang et al.[3], dark green from this study) are superimposed on original normalized profiles (gray).

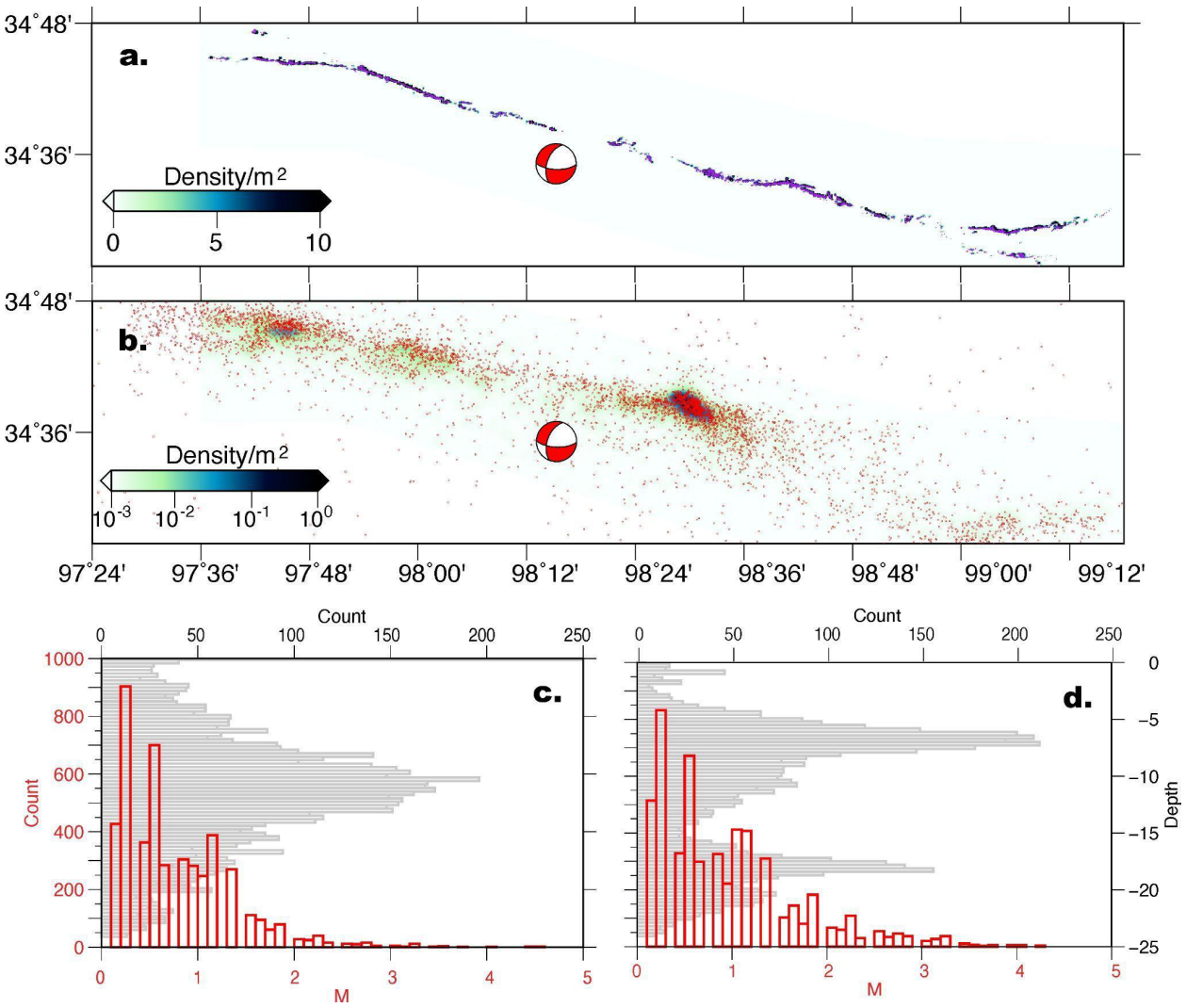

Figure S2. (a) Ground fracture datasets (purple lines) from Liu-Zeng et al.[2] superimposed on the map of fracture density. Fractures are visually digitized using a mosaic of post-earthquake orthorectified photos (spatial resolution: 4–8 cm) from a vertical take-off and landing fixed-wing unoccupied aerial vehicle (UAV). (b) Relocated aftershocks (red circles) within 16 days after the 21 May mainshock (from 21 May 2021 to 7 June 2021), including ~7000 events in total, from Wang et al.[3], superimposed on the map of aftershock density. For the aftershock dataset, the average formal location errors for latitude, longitude, and depth are <0.2, <0.2, and 0.50 km, respectively[3]. (c, d) Comparison of magnitude (red) and depth distribution (gray) of two aftershock catalogs from Wang et al.[3] (c) and generated in this study (d).

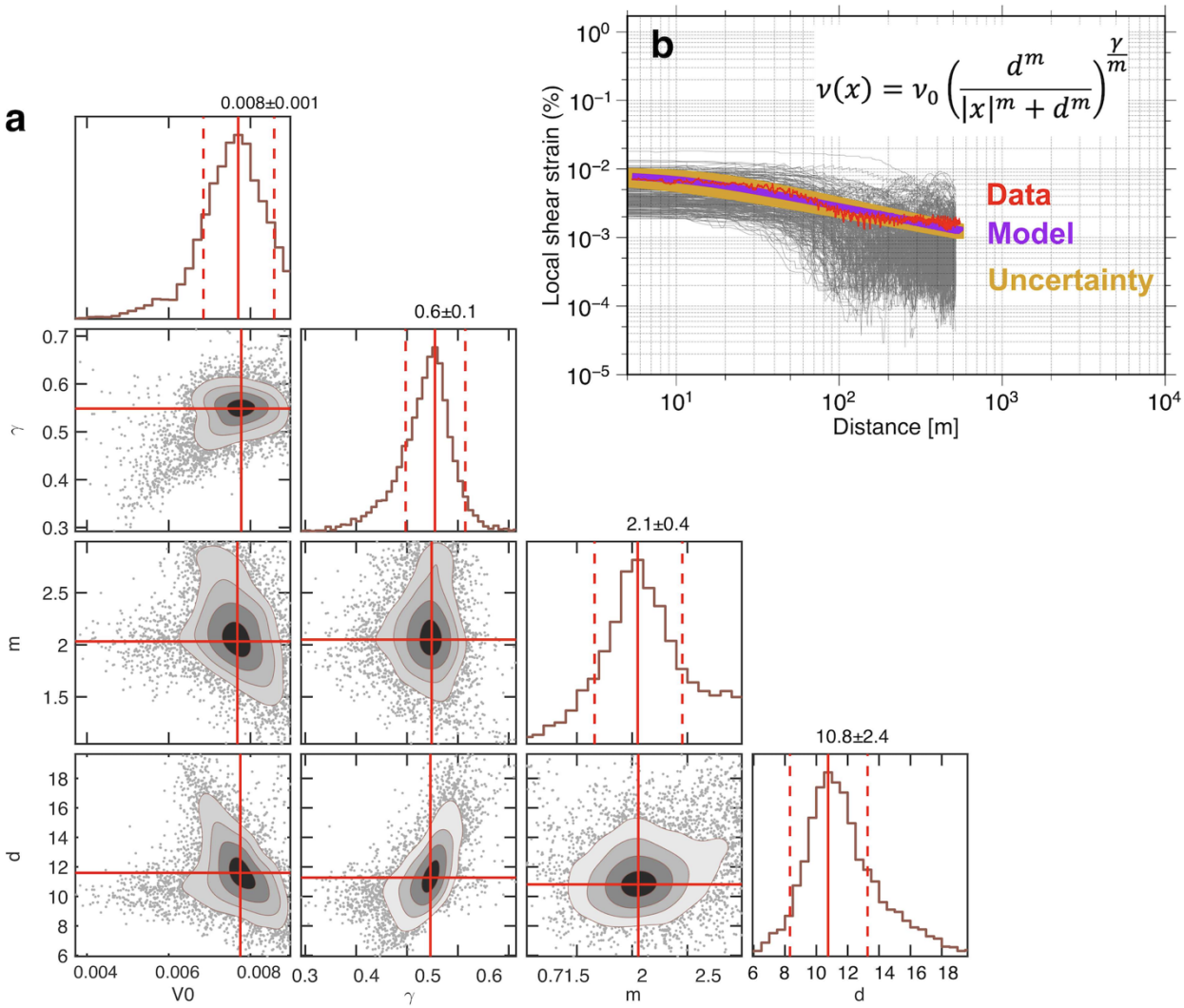

Figure S3. Example showing the fitting result using the inverse power law for surface shear strain profiles. (a) One-dimensional (the diagonal panel in each subplot) and two-dimensional (the panels with grey point cloud) marginal probability distributions of four free parameters in the inverse pow law, v_0, γ, m and d. The red solid line denotes the maximum a posteriori probability (MAP) solution for each parameter. Red dashed lines indicated the 95% confidence interval of the derived probability density functions. The values above each histogram indicate the best-fitting value. (b) fitting result (purple line) using the inverse power law for one normalized, stacked shear strain profile (red).

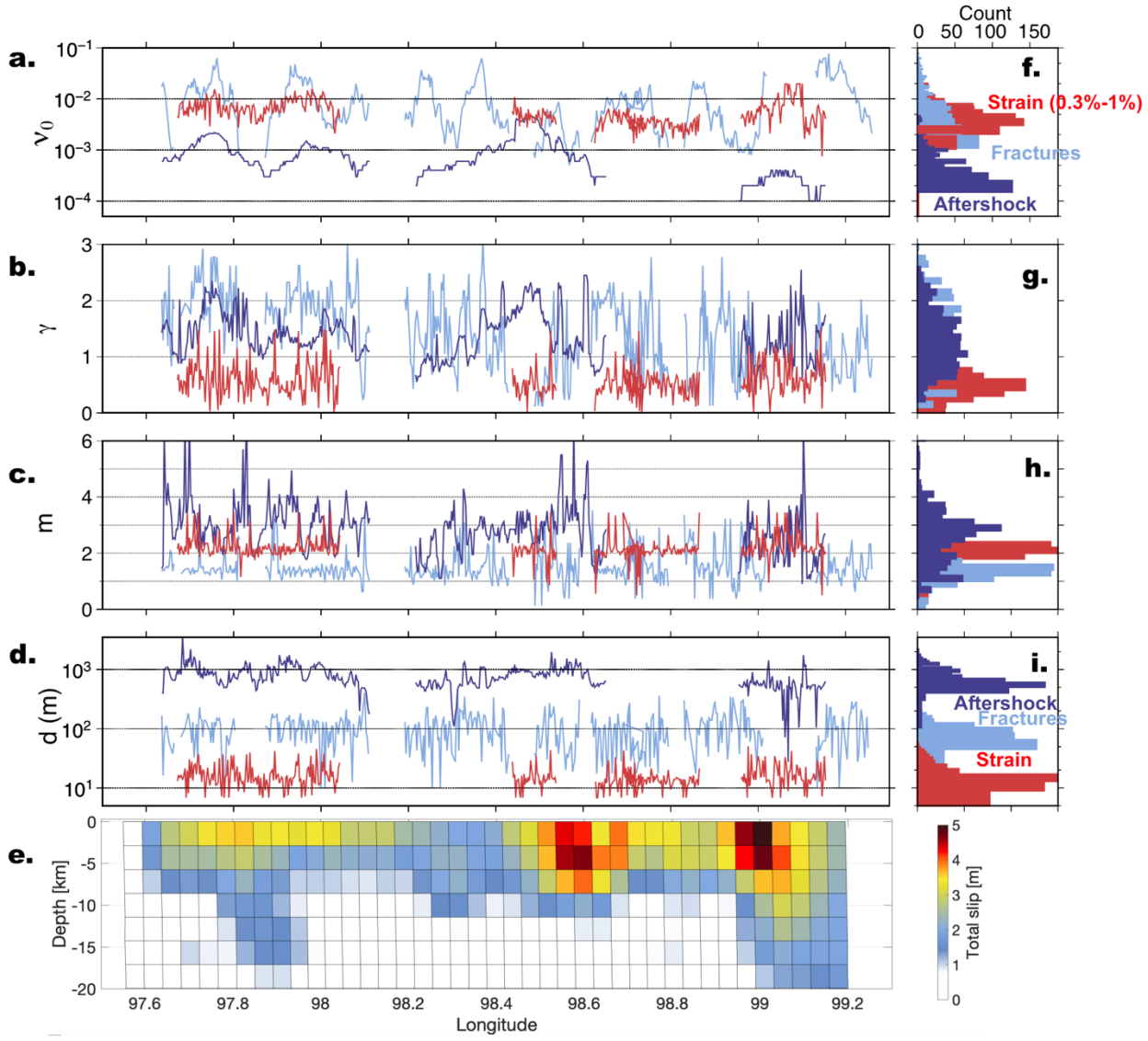

Figure S4. (a, b, c, d) Distribution of the maximum likelihood fitting results of four parameters in the inverse power law for surface shear strain (dark red), fractures (light blue), and relocated aftershocks (dark blue). (e) Kinematic slip distribution inverted from geodetic and seismological data for the Maduo earthquake[4]. (f, g, h, i) Histogram of the four parameters in the inverse power law for surface shear strain (dark red), fractures (light blue), and aftershocks (dark blue).

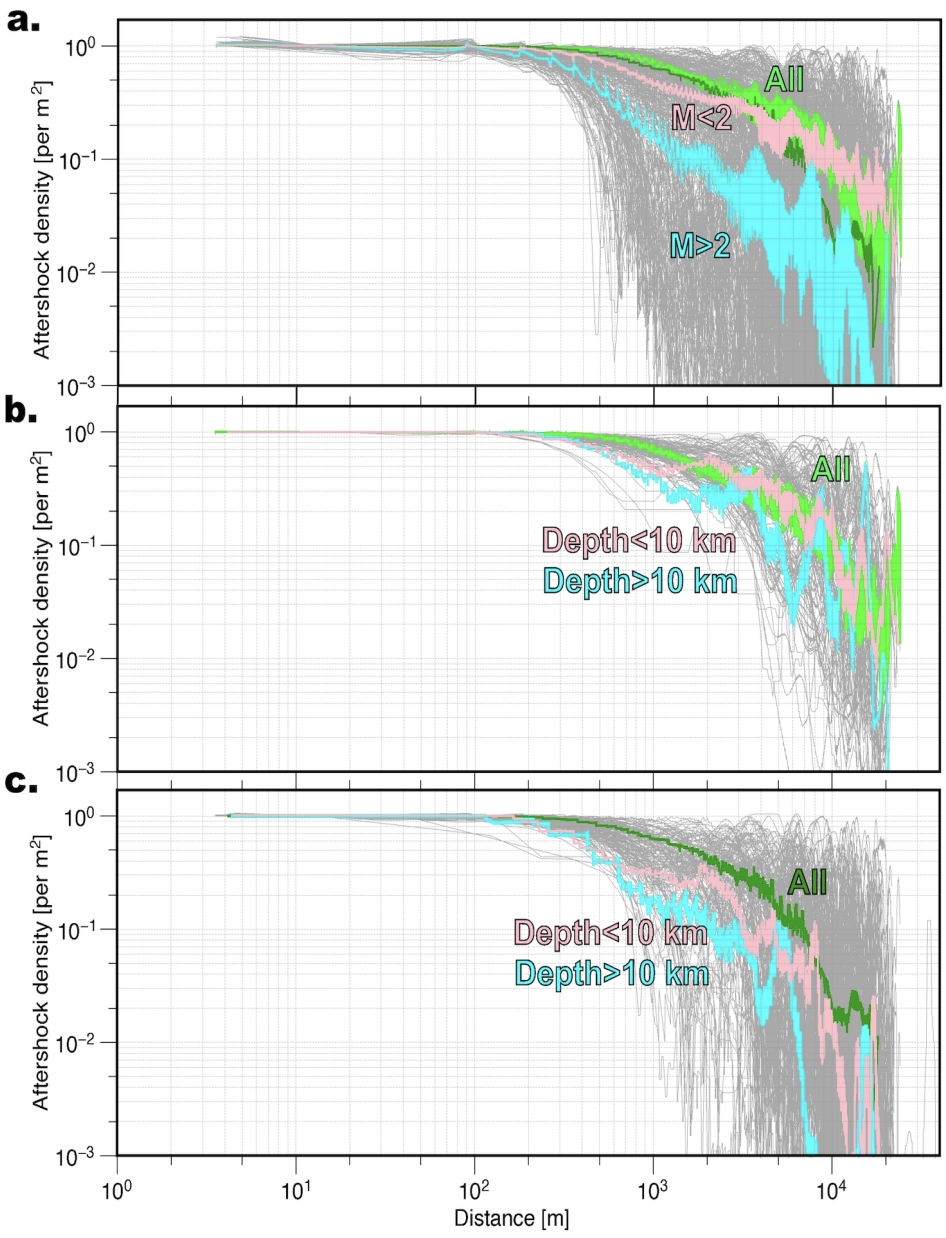

Figure S5. Comparison of normalized decay of aftershocks binned by magnitude (a) and depth (b, c) with fault-perpendicular distance. In a-c, green curves mark the normalized decay of aftershocks based on datasets from Wang et al.[3]. Dark green curves show the normalized decay of aftershocks based on the new datasets in this study. In a, cyan and pink curves mark the normalized decay of aftershocks from Wang et al.[3] with M>2 and M<2, respectively. In b and c, cyan and pink curves mark the normalized decay of aftershocks from aftershocks with depth > 10 km and depth < 10 km, respectively. Gray curves are the normalized decay of aftershock density calculated from a series of fault-perpendicular profiles every 50 m perpendicular to the trace of surface ruptures.

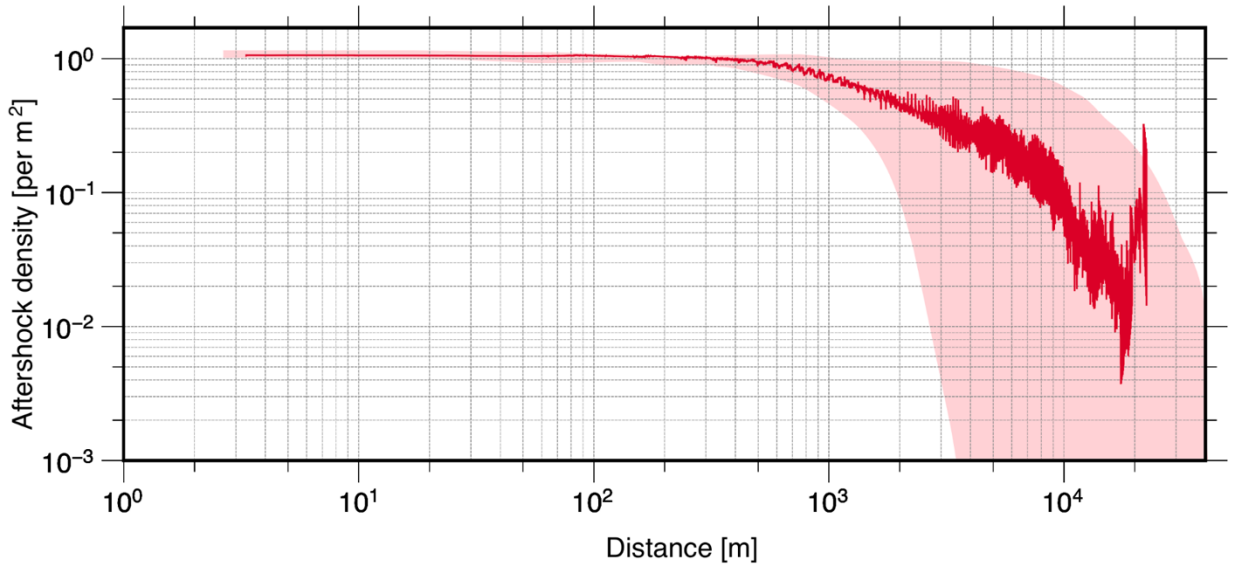

Figure S6. The range of the aftershock density decay curve (pink band), after adding noise of 400 m, representing the hypocentral location uncertainty of aftershock datasets.

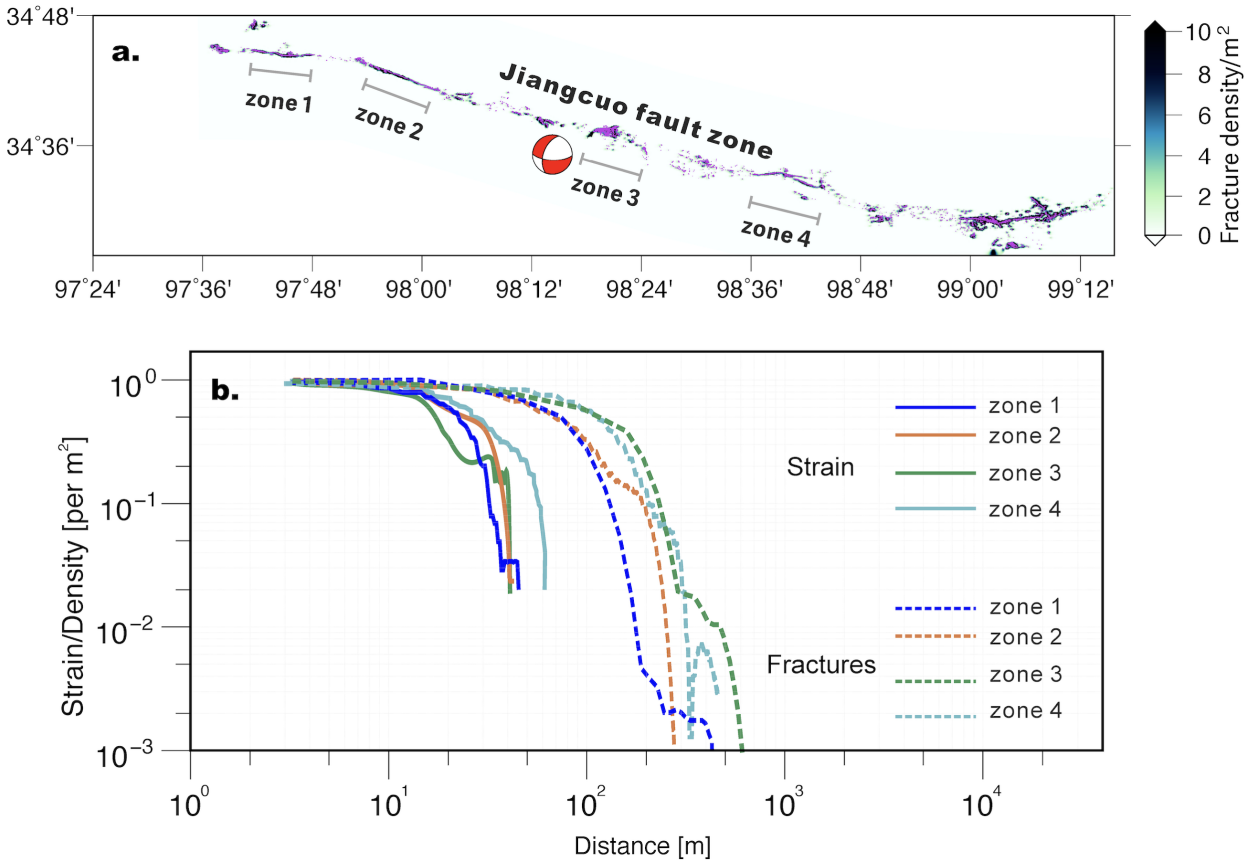

68

69 **Figure S7.** Normalized decay of surface shear strain and fractures along four sections. Zone 1 and
70 zone 2 have limited secondary fractures outside the main rupture zone, while zone 3 and zone 4
71 have small secondary faults and some distributed fractures outside the main rupture zone. (a)
72 shows ground fracture datasets (thin purple lines)[1], which are superimposed on the calculated
73 fracture density.

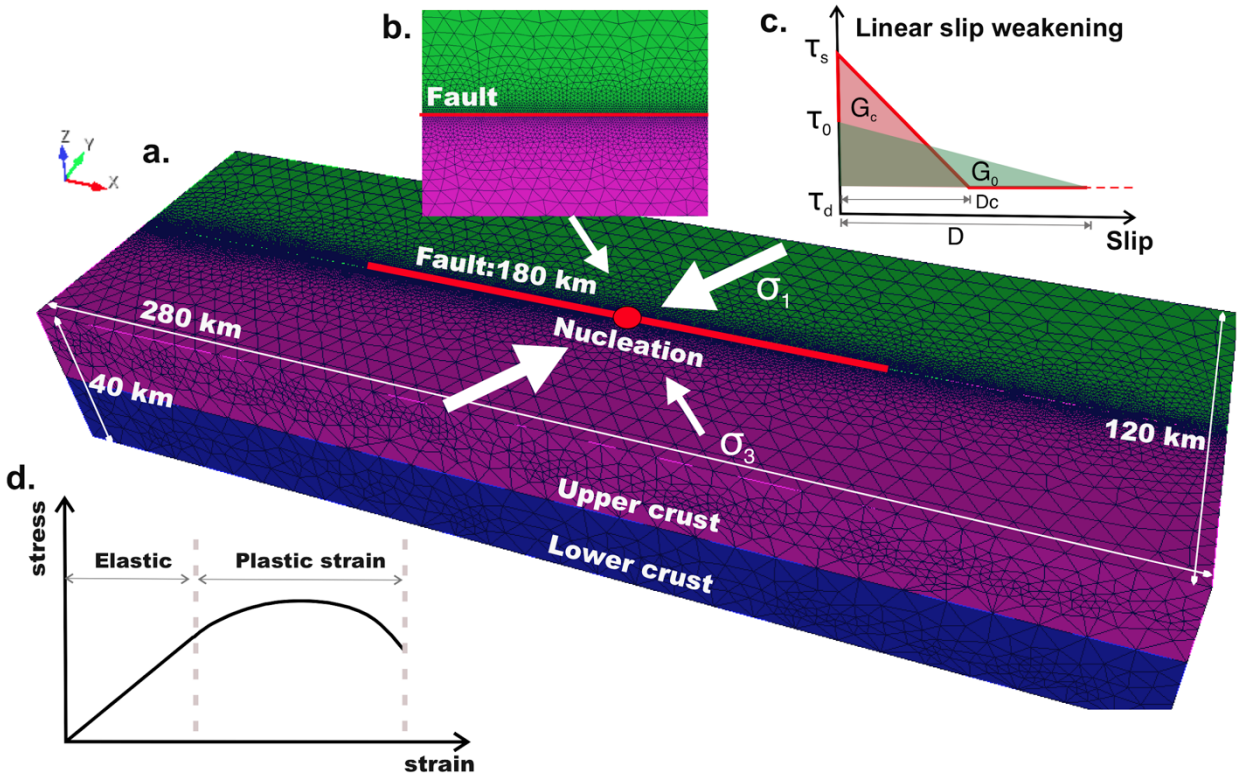

Figure S8. (a, b) Model domain and meshing in Pylith software. The principal compressive stresses σ1 oriented (N060)°/(240) °, σ3 (N330) °/(150) ° are based on the results from Zhang et al.[5], using focal mechanisms of the Maduo mainshock and aftershock sequence. (c) Schematic plot of the fracture energy G_c and the static energy release rate G_0 in the linear slip-weakening friction laws used in our dynamic rupture models. (d) Stress-strain evolution in the Drucker-Prager yield criterion used in this study[6].

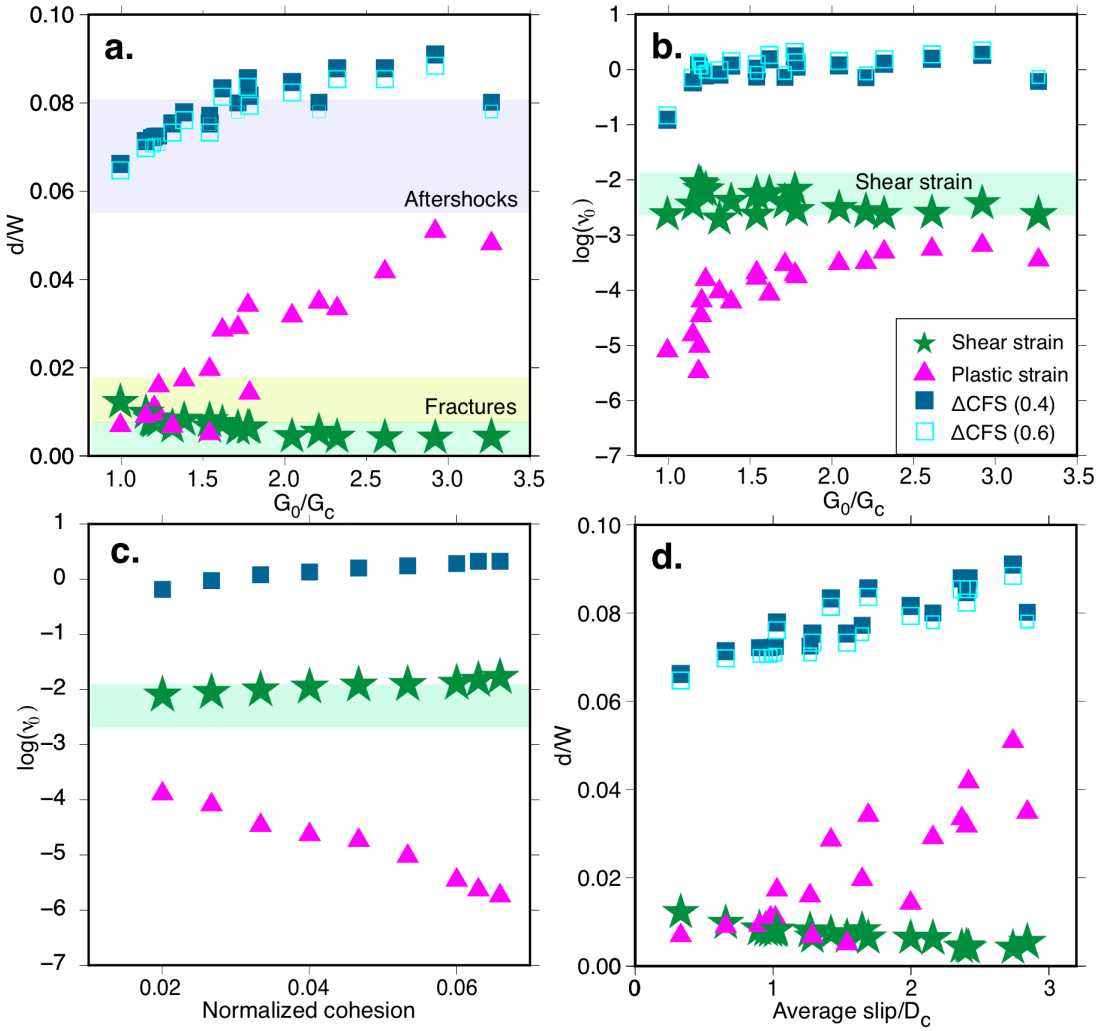

Figure S9. Multiscale fault-zone deformation controlled by energy ratio and cohesion. (a) Normalized d/W from dynamic modeling versus energy ratio (G_0/G_c). (b) Modeled v_0 versus energy ratio (G_0/G_c). In (a), horizontal lines denote the observed average decay distance of aftershocks (700-1000 m; light purple), fractures (100-250 m; light yellow), and surface shear strain (20-100 m; light green), normalized by an average rupture width of 13 km based on kinematic slip model of the Maduo earthquake. The calculations of rupture speeds from each dynamic model are distance-averaged (20-90 km along the strike) steady-state values at a fixed initial rupture speed. In (a, b), dark blue solid and cyan hollow squares are based on the friction coefficient μ =0.4 and 0.6, respectively, when calculating ΔCFS. (c) Modeled v_0 versus normalized cohesion by normal stress (80 Mpa). In (b, c), light green horizontal lines denote the observed v_0 of surface shear strain during the Maduo earthquake. (d) Normalized d/W from dynamic modeling versus normalized average slip by the critical slip-weakening distance Dc.

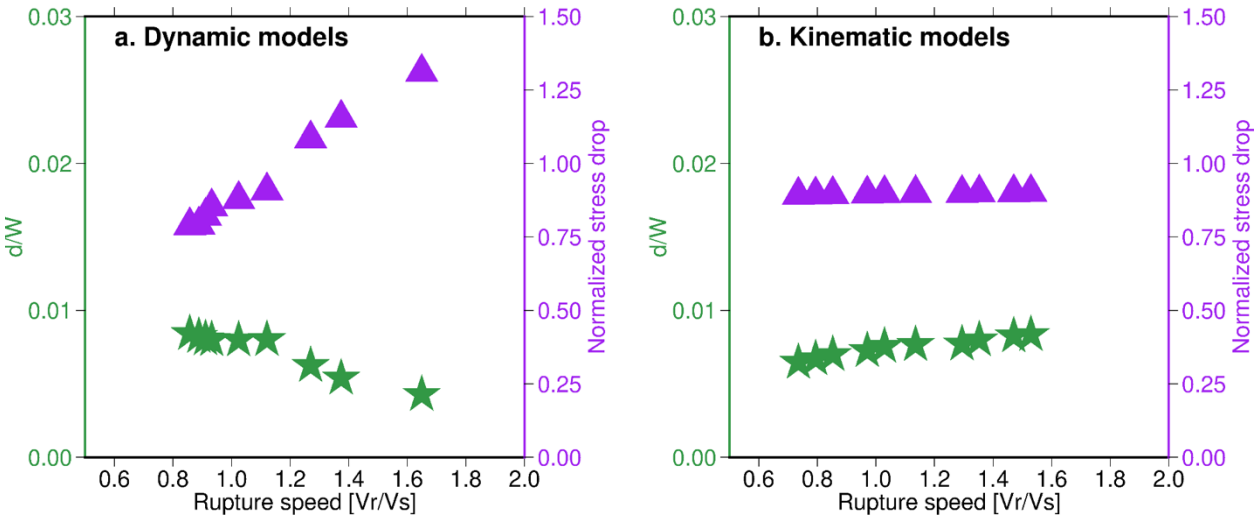

Figure S10. (a) Normalized d/W (dark green) and stress drop (purple) versus rupture speed in dynamic (a) and kinematic (b) models. Stress drops are normalized by static stress drop ($\tau_0 - \tau_d$), values >1 meaning overshooting in dynamic rupture. V_r is rupture speed, and V_s is the S wave speed. In the kinematic models, dynamic wave propagation is incorporated.

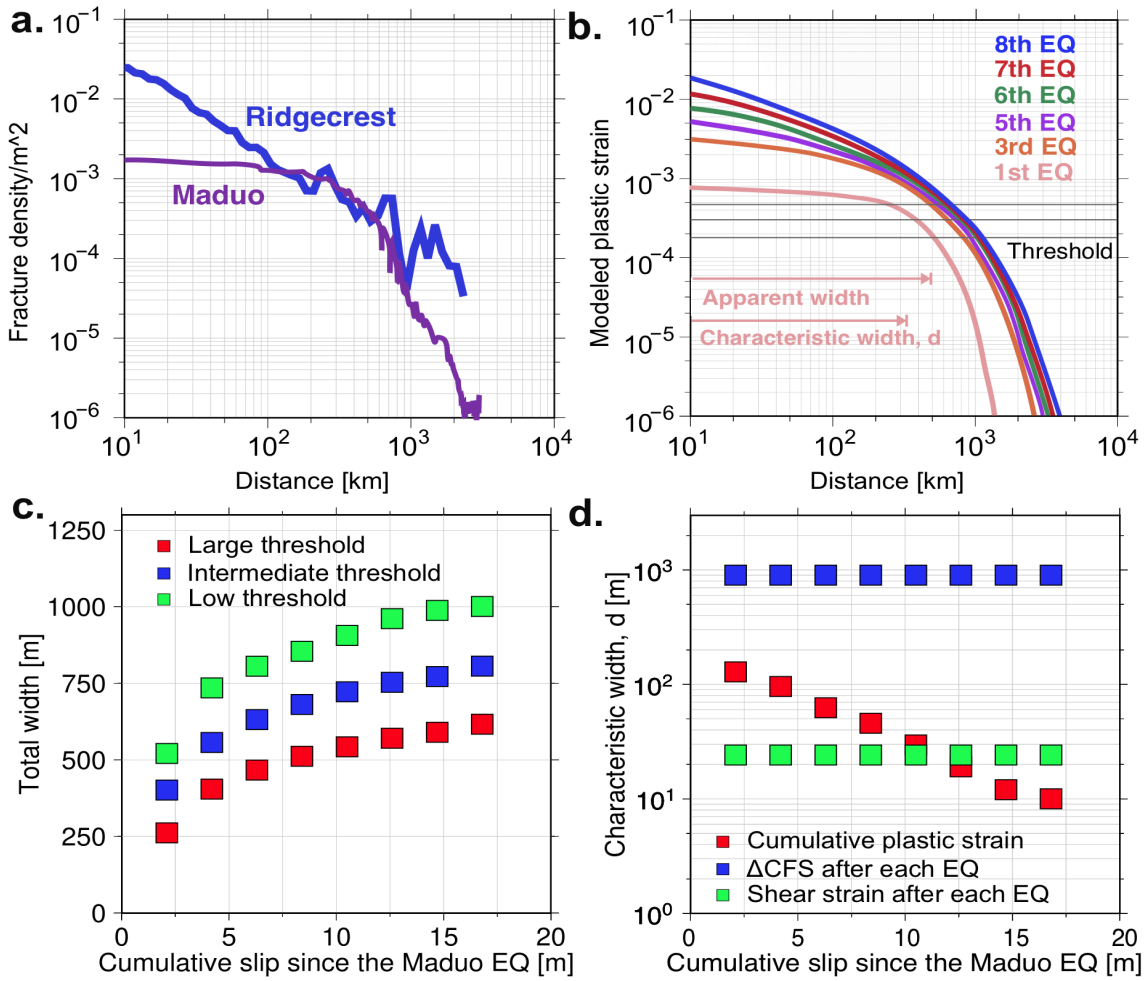

Figure S11. Modeled evolution of cumulative plastic strain accumulation over an eight-earthquake cycle, compared with geodetic observations. (a) Comparison of fracture density decay between the Maduo (purple curve; from this study) and the Ridgecrest earthquake[7] (blue curve). (b) Comparison of accumulated plastic strain distribution in our eight-earthquake cycle model (EQ: earthquake). Three grey horizontal lines mark three applied plastic strain thresholds to determine the total width of the fault damage zone. (c) Evolution of the apparent fault-zone width versus the average cumulative slip on the fault. Three apparent fault-zone widths (green, blue, and red squares) are based on three plastic strain thresholds (shown in b) for each earthquake cycle. (d) Evolution of the characteristic width, d in Eq. 1 in the main text, versus the average cumulative slip on the fault. Note that the total width of the fault damage zone (c) and the decay width (d) are the half-width across the fault damage zone.

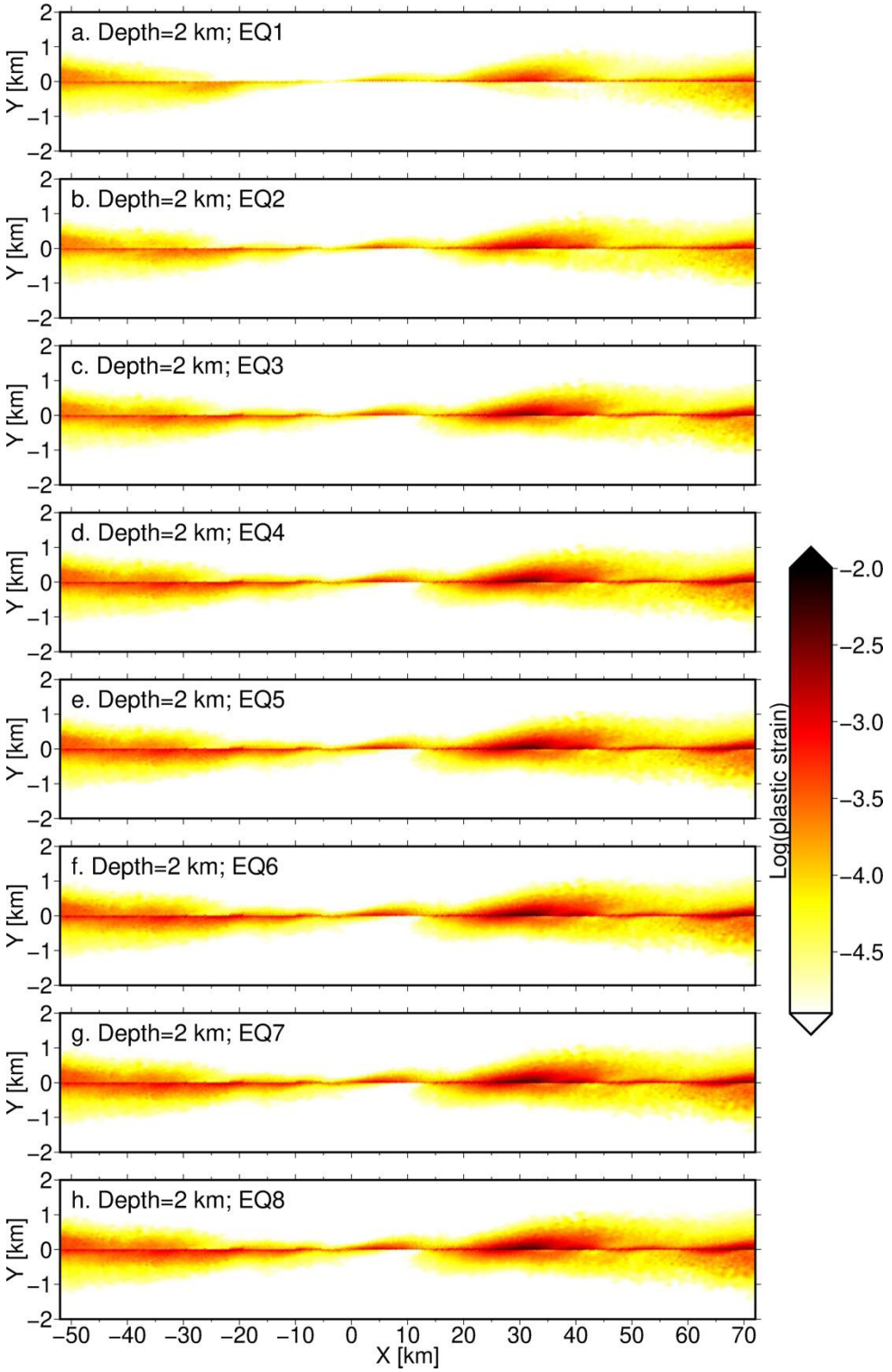

Figure S12. Accumulative plastic strain distribution over an eight-earthquake cycle at a depth of 2 km. In the kinematically constrained model, dynamic wave propagation is incorporated. EQ: earthquake.

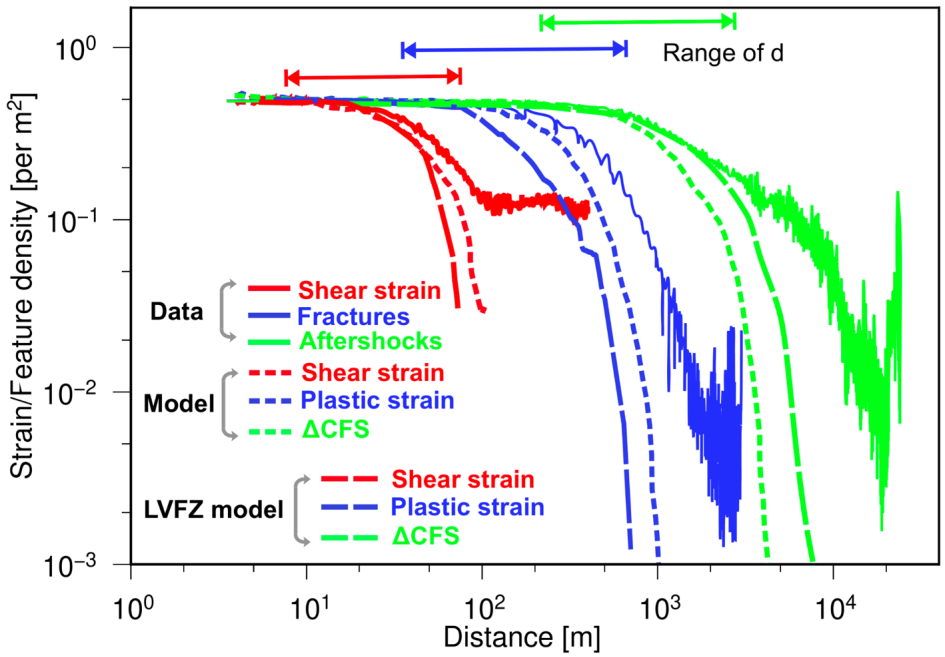

Figure S13. Comparison between the best-fitting dynamic rupture model (short dashed lines) and the one with low-velocity fault zone (LVFZ; long dashed lines). The observed scaling with distance from the fault for surface shear strain, fractures, aftershocks, and the best-fitting dynamic rupture model is the same as **Fig. 2** in the main text.

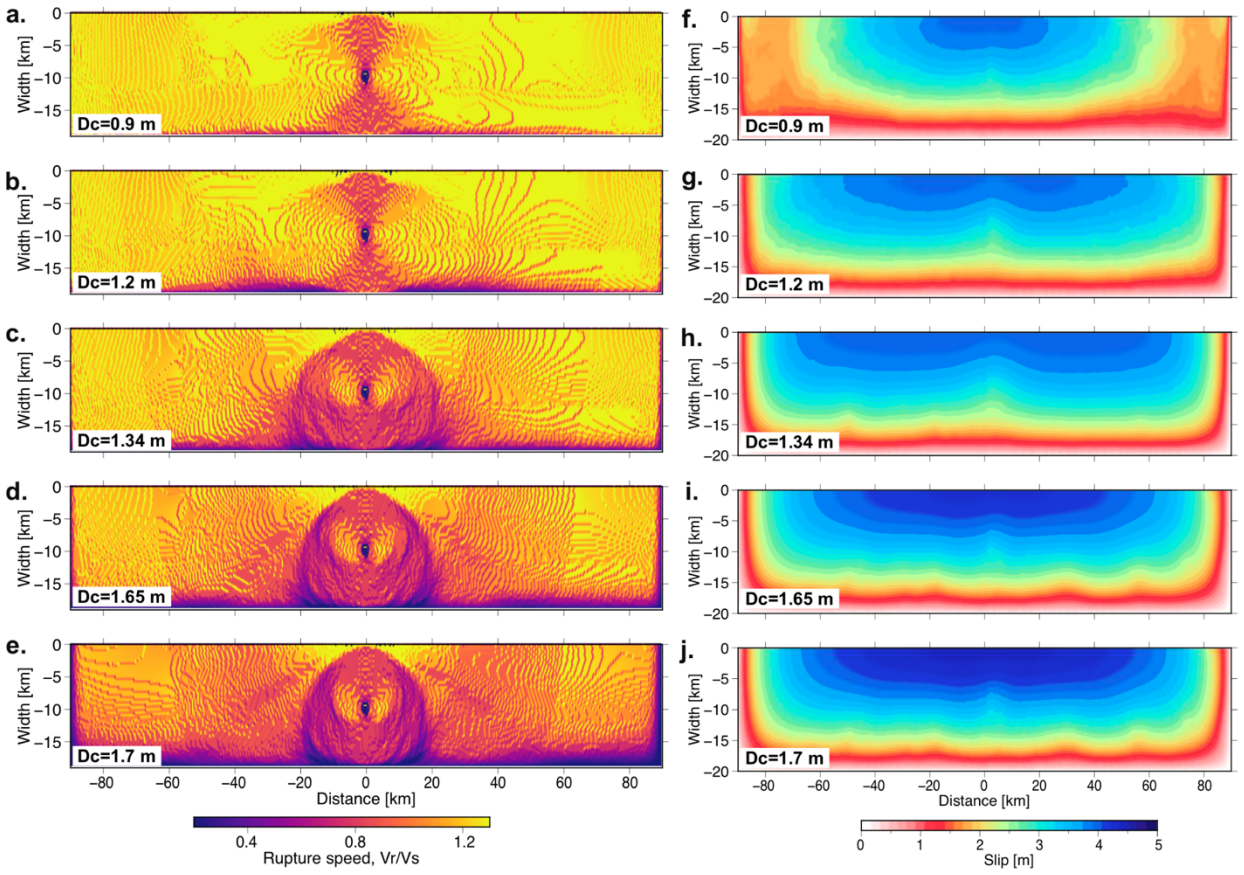

Figure S14. Distribution of rupture speed (V_r) relative to the S-wave speed (V_s) (a-e) and the simulated slip (f-j) by varying Dc in the dynamic models (see detailed parameters in Table S1).

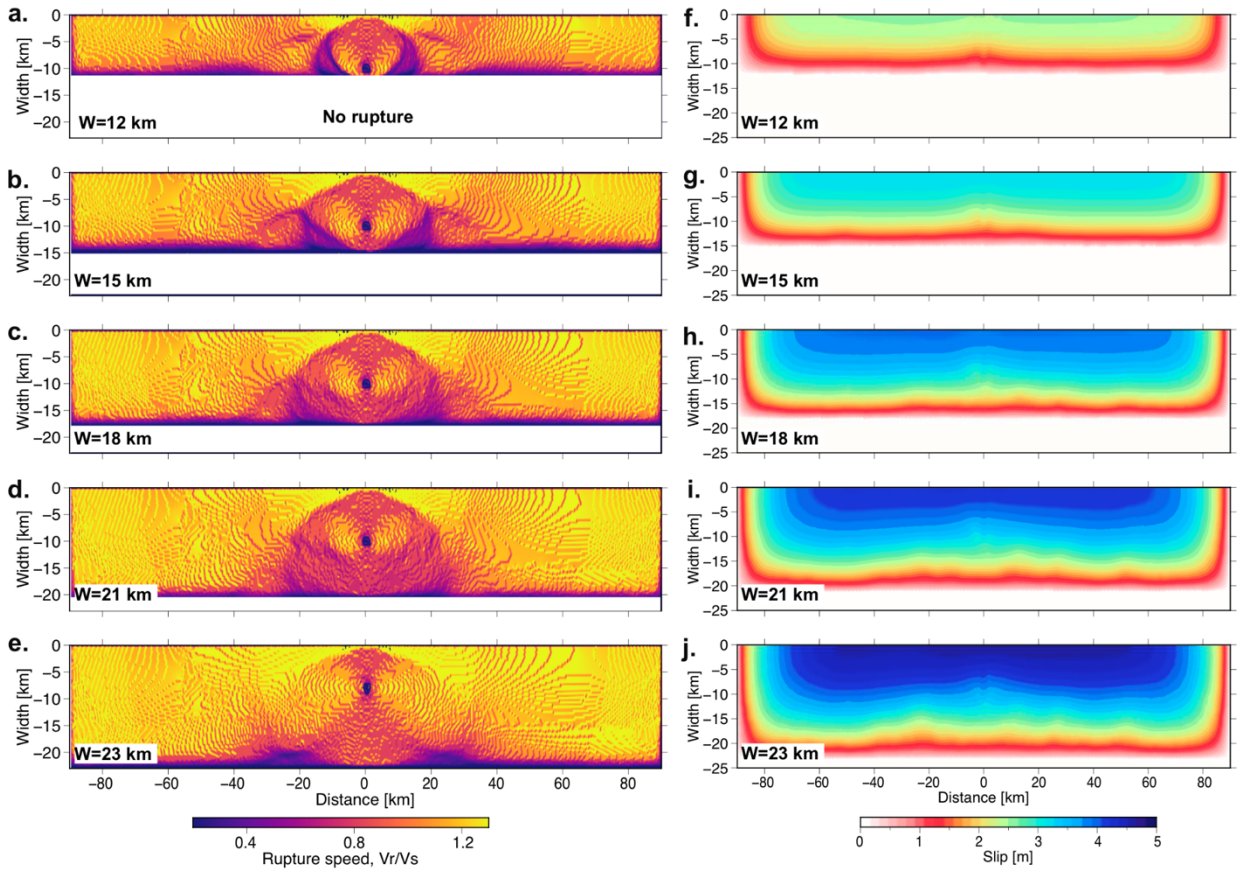

Figure S15. Distribution of rupture speed (V_r) relative to the S-wave speed (V_s) (a-e) and the simulated slip (f-j) by varying rupture width, W, in the dynamic models (see detailed parameters in Table S1).

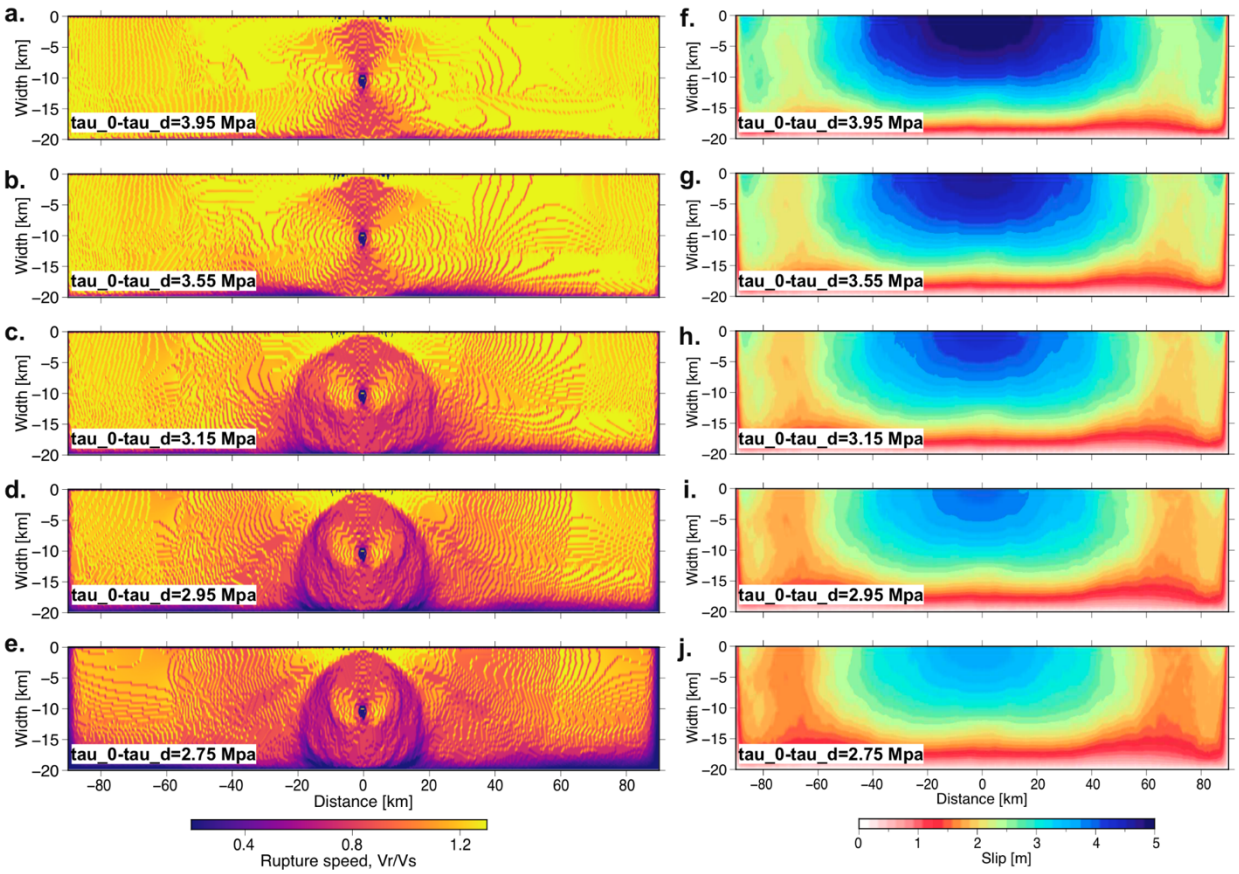

Figure S16. Distribution of rupture speed (V_r) relative to the S-wave speed (V_s) (a-e) and the simulated slip (f-j) by varying static stress drop $\tau_0 - \tau_d$ in dynamic models (see detailed parameters in Table S1).

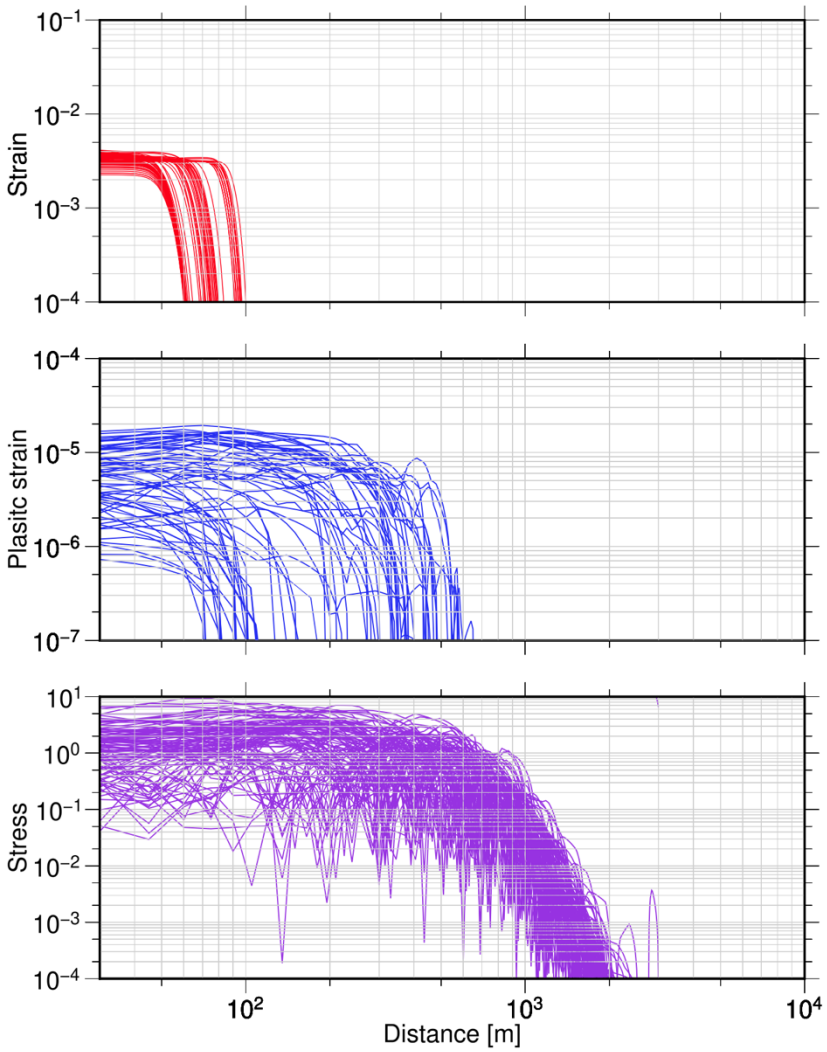

Figure S17. An example showing the decay of surface shear strain (top panel, red curves), plastic strain (central panel, blue curves), and the ΔCFS (bottom panel, purple curves) in the dynamic simulations. The decay of the modeled surface shear strain, plastic strain, and the ΔCFS could be compared to our observations of surface shear strain, fracture density, and aftershock density, shown in **Fig. S1**.

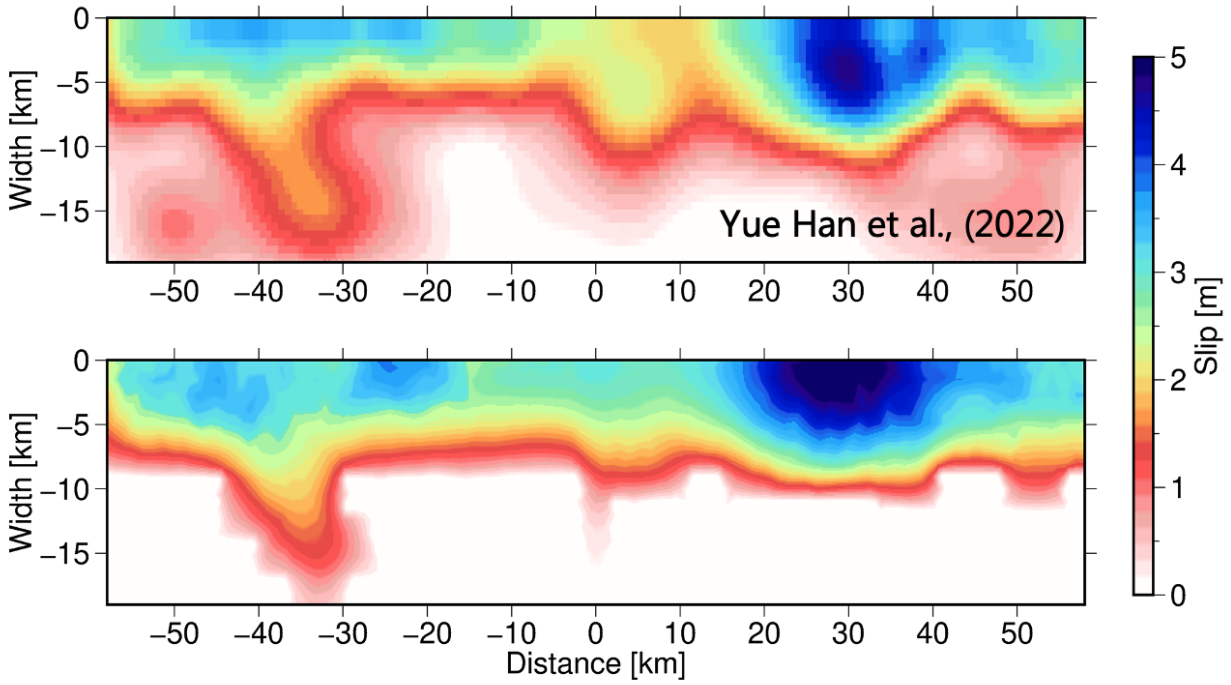

Figure S18. Comparison between the input kinematic slip model[1] as constraints of heterogeneous stress drop $\Delta\tau$ in the simulations and the calculated slip distribution from the dynamic rupture simulations.

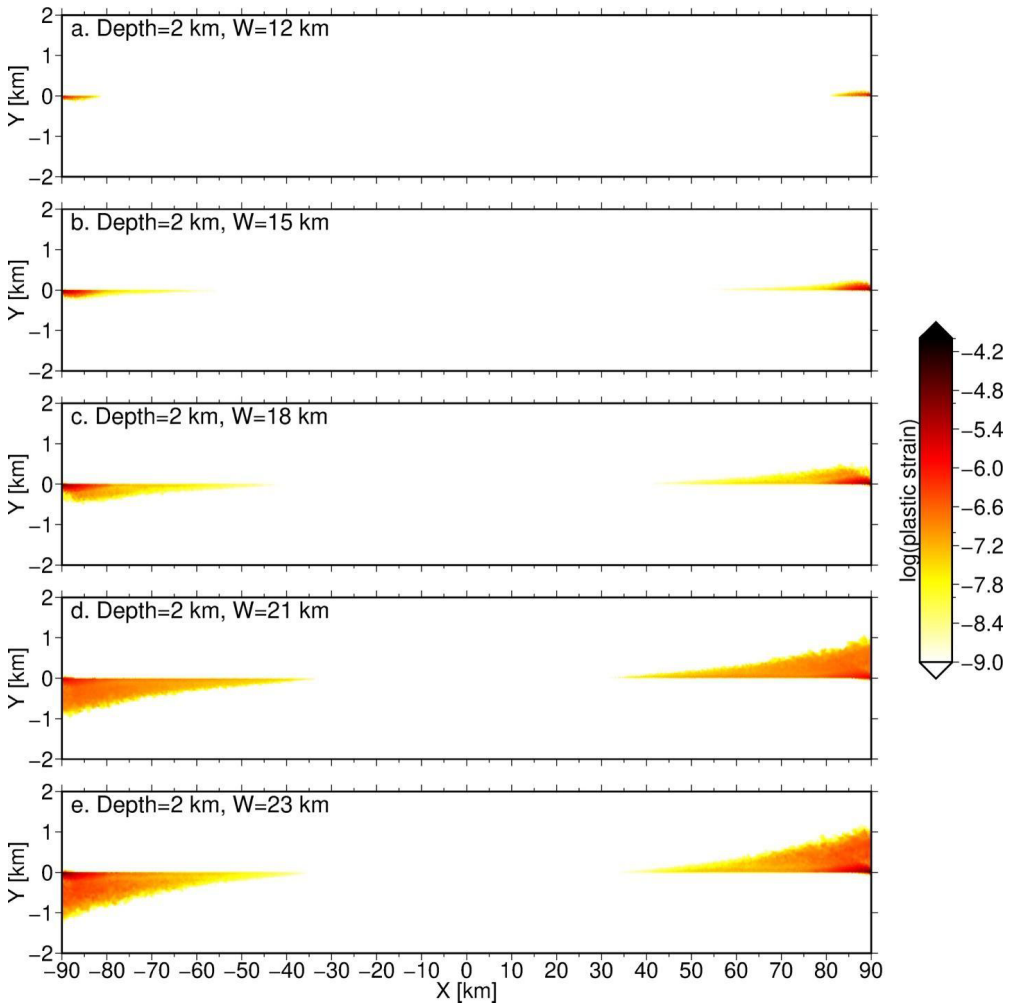

141

142 **Figure S19.** An example showing the effect of the rupture width (W) on the decay distance (d)
143 and intensity (v_0) of the plastic strain in simple dynamic models (Models 2-1 to 2-5 in **Table**
144 **S1**).

Table S1. Detailed parameters used in the simple dynamic rupture models.

	τ_s (Mpa)	τ_0 (Mpa)	τ_d (Mpa)	$\Delta\tau$ (Mpa)	μ_s	μ_d	σ (Mpa)	D_c (m)	W (km)	G_c $/G_0$
Model 1-1	49.6	45	40	5	0.62	0.5	80	**0.65**	20	0.30
Model 1-2	49.6	45	40	5	0.62	0.5	80	**0.9**	20	0.44
Model 1-3	49.6	45	40	5	0.62	0.5	80	**1.2**	20	0.57
Model 1-4	49.6	45	40	5	0.62	0.5	80	**1.34**	20	0.64
Model 1-5	49.6	45	40	5	0.62	0.5	80	**1.65**	20	0.80
Model 1-6	49.6	45	40	5	0.62	0.5	80	**1.67**	20	0.81
Model 1-7	49.6	45	40	5	0.62	0.5	80	**1.69**	20	0.82
Model 1-8	49.6	45	40	5	0.62	0.5	80	**1.7**	20	0.825
Model 1-9	49.6	45	40	5	0.62	0.5	80	**1.71**	20	0.83
Model 2-1	46.8	46.7	42.75	3.95	0.623	0.57	75	2	**13**	0.98
Model 2-2	46.8	46.7	42.75	3.95	0.623	0.57	75	2	**15**	0.85
Model 2-3	46.8	46.7	42.75	3.95	0.623	0.57	75	2	**18**	0.71
Model 2-4	46.8	46.7	42.75	3.95	0.623	0.57	75	2	**21**	0.61
Model 2-5	46.8	46.7	42.75	3.95	0.623	0.57	75	2	**23**	0.55
Model 3-1	46.8	46.7	42.75	**3.95**	0.623	0.57	75	1	20	0.32
Model 3-2	46.8	46.5	42.75	**3.75**	0.623	0.57	75	1	20	0.35
Model 3-3	46.8	46.3	42.75	**3.55**	0.623	0.57	75	1	20	0.39
Model 3-4	46.8	46.1	42.75	**3.35**	0.623	0.57	75	1	20	0.44
Model 3-5	46.8	45.9	42.75	**3.15**	0.623	0.57	75	1	20	0.50
Model 3-6	46.8	45.7	42.75	**2.95**	0.623	0.57	75	1	20	0.57
Model 3-7	46.8	45.5	42.75	**2.75**	0.623	0.57	75	1	20	0.66

Reference

1. Yuan, Z. *et al.* Large Surface-Rupture Gaps and Low Surface Fault Slip of the 2021 Mw 7.4 Maduo Earthquake Along a Low-Activity Strike-Slip Fault, Tibetan Plateau. *Geophys Res Lett* **49**, (2022).
2. Liu-Zeng, J. *et al.* Fault Orientation Trumps Fault Maturity in Controlling Coseismic Rupture Characteristics of the 2021 Maduo Earthquake. *AGU Advances* **5**, (2024).
3. Wang, W. *et al.* Aftershock sequence relocation of the 2021 Ms 7.4 Maduo earthquake, Qinghai, China. *Sci China Earth Sci* **64**, 1371–1380 (2021).
4. Yue, H. *et al.* Rupture process of the 2021 M7.4 Maduo earthquake and implication for deformation mode of the Songpan-Ganzi terrane in Tibetan Plateau. *Proceedings of the National Academy of Sciences* **119**, e2116445119 (2022).
5. Zhang, Z., Deng, Y., Qiu, H., Peng, Z. & Liu-Zeng, J. High-resolution imaging of fault zone structure along the creeping section of the Haiyuan fault, NE Tibet, from data recorded by dense seismic arrays. *J Geophys Res Solid Earth* **127**, e2022JB024468 (2022).
6. Drucker, D. C. & Prager, W. Soil mechanics and plastic analysis or limit design. *Q Appl Math* **10**, 157–165 (1952).
7. Rodriguez Padilla, A. M., Oskin, M. E., Milliner, C. W. D. & Plesch, A. Accrual of widespread rock damage from the 2019 Ridgecrest earthquakes. *Nat Geosci* **15**, 222–226 (2022).